optica

Multifunctional integrated photonics in the mid-infrared with suspended AlGaAs on silicon: supplementary material

JEFF CHILES,[1,*] NIMA NADER,[1] ERIC J. STANTON,[1] DANIEL HERMAN,[1,2] GALAN MOODY,[1] JIANGANG ZHU,[3] J. CONNOR SKEHAN,[1,†] BISWARUP GUHA,[4,5] ABIJITH KOWLIGY,[6,2] JULIET T. GOPINATH,[2,3] KARTIK SRINIVASAN,[4] SCOTT A. DIDDAMS,[6,2] IAN CODDINGTON,[1] NATHAN R. NEWBURY,[1] JEFFREY M. SHAINLINE,[1] SAE WOO NAM,[1] AND RICHARD P. MIRIN[1]

[1] *NIST, Applied Physics Division, 325 Broadway, Boulder CO 80305, USA*
[2] *CU Boulder, Department of Physics, Boulder CO 80309, USA*
[3] *CU Boulder, Department of Electrical and Computer Engineering, Boulder CO 80309, USA*
[4] *NIST, Center for Nanoscale Science and Technology, 100 Bureau Dr, Gaithersburg, MD 20899, USA*
[5] *Maryland Nanocenter, University of Maryland, College Park, MD 20742, USA*
[6] *NIST, Time and Frequency Division, 325 Broadway, Boulder CO 80305, USA*
[†] *Now with EPFL, Route Cantonale, 1015 Lausanne, Switzerland*
[*] *jeffrey.chiles@nist.gov*

Published 18 September 2019

This document provides supplementary information to "Multifunctional integrated photonics in the mid-infrared with suspended AlGaAs on silicon," https://doi.org/10.1364/optica.6.001246 In Section 1, we discuss experimental results for unpassivated waveguides. In Section 2, we analyze sources of propagation loss in the mid-IR. In Section 3, we discuss the damage threshold and physical robustness of suspended AlGaAs waveguides. In Section 4, we consider miscellaneous details pertaining to the design and fabrication of the devices. In Section 5 we elaborate on the measurement setups for the passive and nonlinear characterization.

1. Characterization of unpassivated waveguides

If no passivation is used on the AlGaAs waveguide surfaces, it will very rapidly form a native oxide layer consisting of various phases of arsenic, gallium and aluminum oxides. In the near-IR, the resulting losses of this reconstruction layer are noticeable on the level of 1 dB/cm for nanoscale waveguides [1]. However, the effects of this layer on photonic devices have not yet been studied in the mid-IR. We tested several devices without SiN passivation to better understand its effects on these waveguides. The results are summarized in Table S1. In the first test, an unpassivated waveguide from an earlier fabrication run (core thickness 350 nm, waveguide width of 2.2 μm) was tested via cutback at λ = 3.4 μm to find the propagation loss once the surface was fully oxidized (after weeks in atmosphere). The loss was so high that it could only be measured with 0.9 mm propagation length difference using a microbolometer array to resolve the faint out-coupled modes. A propagation loss > 100 dB/cm was observed. Next, we examined a different waveguide (core thickness 540 nm, waveguide width of 2.2 μm) which was only passivated on the bottom surface. We stripped the top oxide using ammonium hydroxide and hydrochloric acid, then measured the loss roughly 1 hour later. We recorded a loss of 16 dB/cm. Finally, we examined the loss at λ = 4.6 μm using ring resonator measurements. The device under consideration had a core thickness of 540 nm, a ring waveguide width of 2.7 μm, and only bottom-side passivation similar to the previous example. A loss of 5.5 dB/cm was observed about 30 minutes after the top-oxide strip.

A few conclusions may be drawn from these data. The first is that unpassivated AlGaAs waveguides exhibit substantial absorption losses near λ = 3.4 μm. Secondly, it does not take

much time for the losses to increase to unacceptable levels, meaning that even laboratory-scale demonstrations of similar platforms should count on implementing passivation prior to measuring devices. Finally, the lower loss observed at $\lambda = 4.6$ μm suggests that there is significant structure to the absorbance spectrum of the surface states, although it is still problematic well beyond the spike in loss observed near $\lambda = 3.4$ μm. This absorbance feature is worthy of future study to highlight its chemical origins, since it does not correspond to any previously observed feature in the absorption spectra of gallium or arsenic oxides [2]. Note that in Ref. [2], the absorption feature near $\lambda = 3$ μm is due to water contamination in the samples, and should not be interpreted as an intrinsic feature of the materials.

2. Mid-IR loss contributions

In the main manuscript, we characterized the performance of microring resonators over a spectrum spanning from $\lambda = 1.26 - 4.6$ μm. In this section of the Supplement, we consider potential contributions to loss in the mid-IR. Free-carrier absorption could be a factor, given that it generally exhibits loss that increases with wavelength. However, reasonable estimates based on a background carrier concentration of $1 \times 10^{15} cm^{-3}$ put the estimated free-carrier absorption at $\lambda = 5$ μm at a value of < 0.1 dB/cm [3]. Another potential source of loss is the SiN passivation layer, with a total thickness of 30 nm (10 nm on bottom surface, 20 nm on top). First, we measured via prism coupling a bulk material loss of < 2 dB/cm at $\lambda = 1550$ nm for the SiN film by itself, indicating reasonably good film quality. To test the performance in the mid-IR, we performed a differential measurement by depositing 20 nm of additional SiN material on a spiral waveguide cutback with known propagation loss. Measuring at $\lambda = 3.4$ μm, we observed an increase in propagation loss of roughly 1-2 dB/cm. Since the optical mode overlap in the nitride film is only 2%, the equivalent bulk SiN loss at $\lambda = 3.4$ μm is on the order of 50-100 dB/cm.

Since this value is almost two orders of magnitude larger than the losses measured at $\lambda = 1550$ nm, we investigated further with Fourier-transform infrared spectroscopy (FTIR). A SiN film 80 nm thick was deposited on a double-side-polished float zone silicon substrate and measured along with a reference silicon substrate. The sample was oriented at 50° with respect to the illumination axis to minimize reflections. The transmission spectrum, after baseline, reference, and water vapor corrections, is shown in Fig. S1(a). A clear absorption signature is present near $\lambda = 3$ μm, which is most likely due to N-H bonds. Although the SiN film was sputtered without any hydrogenated precursors (specifically to avoid N-H bond contamination), it is possible that some hydrogen was incorporated from the residual gas background of the vaccuum chamber. In Fig. S1(b), the absorption near $\lambda = 3$ μm is zoomed in to illustrate its shape. Evidently, some absorption loss from the N-H bond is still present even at $\lambda = 3.4$ μm, which would explain the strong impact on loss measurements at that wavelength. We note that this sample was not annealed (which was crucial to reducing SiN losses), so it may not exhibit exactly the same characteristics as the films on the final samples. Next, we measured loss using the DFG pump source used for mid-IR supercontinuum ($\lambda = 3.06$ μm). Cutback measurements of paperclip-style 1.8 μm-wide waveguides revealed a loss of 10 dB/cm (Fig. S1(c)), confirming the stronger

Table 1. Summary of loss measurements for unpassivated waveguides.

λ (nm)	Loss	Passivation	Time delay after oxide strip	Method
3400	>100 dB/cm	none	weeks	cutback
3400	16 dB/cm	bottom side only (SiN)	1 hr	cutback
4560	5.5 dB/cm	bottom side only (SiN)	30 min	ring resonator

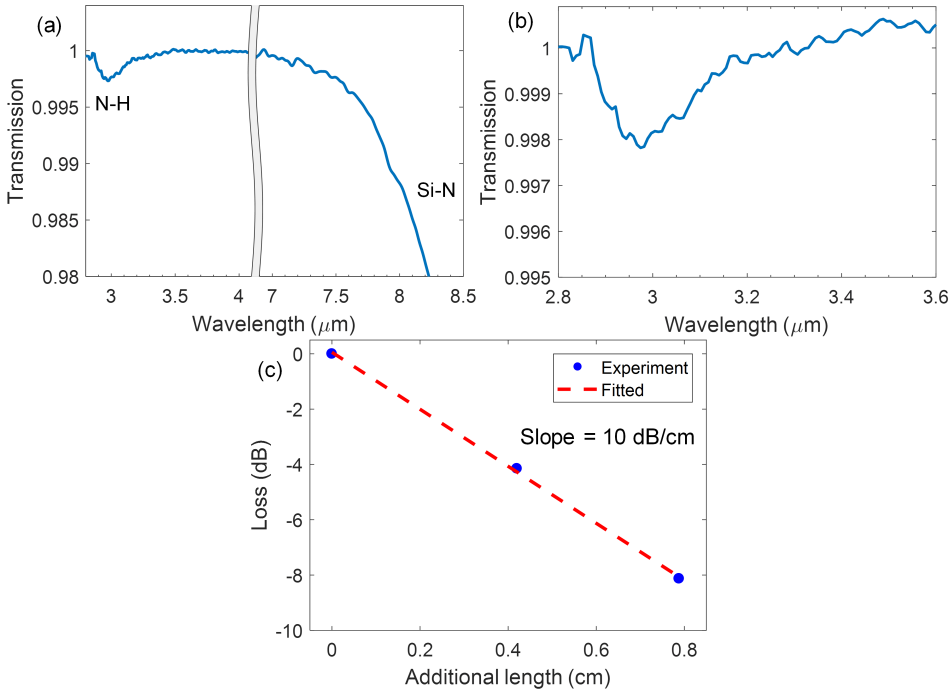

Fig. 1. (a) FTIR measurement of a thin sputtered SiN film, showing transmission dips from N-H and Si-N absorption features. (b) Zoom of the N-H absorption feature. (c) Measurement of the propagation loss at $\lambda = 3060$ nm via paperclip cutback structures (waveguide width of 1.8 μm).

absorption effects for photon energies closer to the N-H resonance.

Finally, we used the FTIR measurements to estimate the limit of transparency achieved with this passivation strategy. In Fig. S1(a), a drop in transmission is visible for $\lambda > 7.3$ μm. This roll-off results from a Si-N stretch resonance, an unavoidable feature of this material [4]. However, the technique used to realize our suspended waveguides can be readily adapted for other passivation materials with much wider transparency windows. For example, zinc sulfide (ZnS) is transparent out to $\lambda = 13$ μm, at which point multi-phonon absorption causes it to become opaque [5]. Future work will employ this or similar materials to fully unlock the transparency window of suspended AlGaAs.

3. Damage threshold and physical robustness

During the 1550 and 3060 nm pumped supercontinuum experiments, we kept note of the average power levels at which the input edge coupler of a waveguide was damaged. For 1550 nm pumping, an average incident (prior to coupling) power level of 14 mW was just enough to damage some waveguide facets. Considering the lens NA of 0.6, the 160 MHz pump repetition rate, and the pulse duration of 61 fs, this translates to a critical peak intensity of 117 GW/cm^2 for a Gaussian beam centered at the facet of the waveguide. For this calculation, we use Eq. S1 to relate the intensity at the center of a Gaussian beam to its total power:

$$I_0 = \frac{2P_0}{\pi w_0^2}, \tag{1}$$

where I_0 is the intensity at the center of the beam, P_0 is the total power (the peak power of the pulse, in our situation), and w_0 is the beam waist at the focal point, related to the NA through Eq. S2:

$$w_0 \approx \frac{\lambda_0}{\pi \mathrm{NA}}, \tag{2}$$

where λ_0 is the free-space wavelength of the beam, and NA is the numerical aperture of the focusing optic used for the measurement (assuming the aperture is completely filled). In earlier experiments, we also tested pumping of the waveguides with a stretched pulse of duration estimated to be 220 ± 50 fs using a lensed fiber (NA = 0.5). In this case, the maximum average power that could be tolerated increased to 70 mW. The corresponding critical peak intensity would be 113 GW/cm^2, which corresponds well with the critical intensity for the fully compressed pulse. This suggests the failure mechanism is more dependent on peak than average power levels in the regime considered here. Finally, we also performed the same analysis for pumping at λ = 3060 nm. An average incident power level of 35 mW was enough to cause facet damage. Considering the lens NA of 0.56, the 100 MHz pump repetition rate, and the pulse duration of 85 fs, this translates to a critical peak intensity of 76 GW/cm^2 at the facet of the waveguide. This places it close to the value observed for the 1560 nm case.

The suspended membranes exhibited excellent mechanical stability during the fabrication process and subsequent experiments. They do not collapse during solvent cleaning or aggressive nitrogen drying in ambient atmosphere, so it is not necessary to use vapor-phase treatments at any point. Prior to die release from the wafer, the membranes underwent heating to 180°C during the pre-bake of the electron-beam resist. Despite the hot air sealed in the sub-surface trenches producing a substantial force against the membranes, they were not damaged. Finally, considering the temperature limit of the individual chips, the maximum tolerable temperature (above which material defects appear) is approximately 450°C, limited by thermal expansion mismatch between the materials.

4. Miscellaneous

In this section, we discuss additional details on the design, fabrication and characterization of the structures and devices considered in the manuscript.

4.1. Epitaxial growth

We started with an epi-ready (100) GaAs wafer and performed oxide removal using an argon-hydrogen plasma in the molecular beam epitaxy (MBE) system's ultrahigh vacuum preparation chamber. The wafer was then transferred to the main growth chamber of the MBE system. First a 250 nm GaAs buffer layer was grown, followed by a 150 nm etch stop layer of $Al_{0.80}Ga_{0.20}As$. A 550 nm device layer of $Al_{0.32}Ga_{0.68}As$ completed the structure. The device layer thickness drops to approximately 540 nm after several oxide removals during the processing. The background doping of this device layer was not directly measured, but previous wafer runs have exhibited background carrier concentrations of less than 1×10^{14} cm^{-3} for GaAs epilayers, indicating the high material quality from this MBE system.

4.2. Surface passivation process

A key element of the fabrication process in this work is the surface passivation. The following procedure was applied for both the top and bottom surfaces of the AlGaAs membrane: (1) ammonium hydroxide oxide removal, (2) hydrochloric acid oxide removal, (3) immediate transfer and evacuation of the load-lock of a sputtering tool, and (4) RF reactive sputtering of silicon nitride. For the sputtering, a platen plasma power of 10 W was applied to the substrate holder, and a silicon target was sputtered with 140 W of plasma power under under argon and nitrogen

flow (nitrogen at 22% of the flow rate of the argon) to form silicon nitride on the surface of the sample, at a pressure of 3 mTorr. The sputtering was performed at room temperature with a base chamber pressure of $< 1 \times 10^{-6}$ Torr. A growth rate of 0.5 nm/min was observed.

4.3. Plasma etching

Next, we consider the plasma etching conditions and their impact on the waveguide geometry. We utilized boron trichloride (BCl_3) and argon (Ar) chemistry in an inductively-coupled plasma (ICP) etching chamber. The ICP power was 350 W, the platen power was 50 W, the pressure was 5 mT, the BCl_3 flow rate was 5 sccm and the Ar flow rate was 20 sccm. A typical waveguide sidewall angle obtained after etching was 86 degrees (positive slope). Additionally, a "foot" near the base of the waveguide core was always observed, giving an increased slab thickness in the vicinity of the core. This was factored into critical calculations such as the waveguide dispersion for supercontinuum generation. Because of this feature, the slab region within gaps < 600 nm was abnormally thick. For example, instead of a typical slab thickness of 90 nm, it was closer to 150 nm near the waveguide core's sidewall region, so we expect the effective slab thickness to vary between those two values as the gap is varied, though we did not directly image this. If a transition between gapped waveguides is made too quickly, this could result in additional radiative losses due to modal mismatch. Partly for this reason, we used pulley couplers for the microring resonators considered in the manuscript, which allow a more gradual transition to the gap region. Since some ring devices were measured over more than an octave of bandwidth, however, they also served to enable sufficient coupling over a wider frequency range than single-point couplers. Further details can be found in Ref. [6].

4.4. Multimode waveguides and applications

We also comment on the use of multimode waveguides for many of the ring resonators measured. In targeted applications such as resonantly-enhanced evanescent sensing, it is usually desirable to carefully design the coupler region, the bus waveguide, and the ring waveguide to concentrate the coupling into a given mode and minimize losses or reductions to the intensity contrast. For the purposes of this work, however, microring resonators were used as a diagnostic tool for accurately measuring propagation loss, rather than a functional device for such applications. With lower propagation losses, smaller waveguide core widths could be used in the rings while maintaining a high Q to make mode management more straightforward, if desired. However, for non-resonant (single-pass) evanescent sensing, as well as supercontinuum generation, the use of multimode waveguides is not an issue for performance, since light can be confined to a single spatial mode through appropriate use of adiabatic tapers and sufficiently gradual, low-loss bends (such as those demonstrated in this work).

4.5. Thermal shift in resonant structures

Next, we briefly consider the thermal properties of the ring resonators. Due to the thin mechanical support connecting the waveguide core to the substrate, they are expected to exhibit considerable thermal resistance, which can be beneficial or detrimental depending on the application in mind. For example, highly efficient thermo-optic modulation could be achieved, but dissipative Kerr soliton generation would be more difficult due to the large resonance shift for different circulating optical powers. We performed a characterization of this thermal shift in a ring resonator with 50 μm radius as shown in Fig. S2. The loaded Q of the resonator was 2.9×10^5, with an extinction ratio of 4 dB. At 1.5 μW waveguide-coupled power (in the bus waveguide outside the ring), the resonance exhibited no noticeable thermal triangle. When the on-chip power was increased to 89 μW, a thermal red-shift of 5 GHz was observed. The large shift is mainly due to the wide membrane (about 11 μm), which dominates the thermal resistance. This width was chosen for low-loss operation at longer wavelengths in the mid-IR, but for applications requiring better

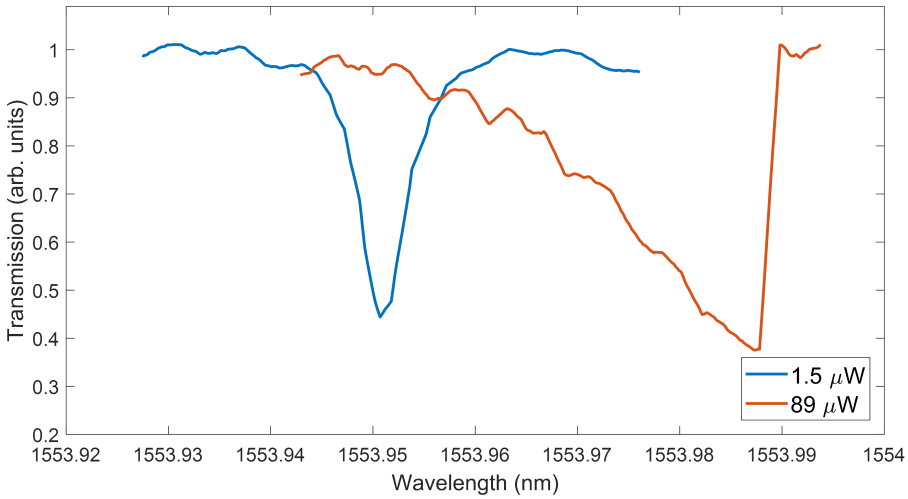

Fig. 2. Characterization of the thermal resonance shift observed in a 50-μm radius resonator. (a) Cold cavity resonance trace for 1.5 μW waveguide-coupled power; (b) Thermally shifted resonance at a higher power of 89 μW.

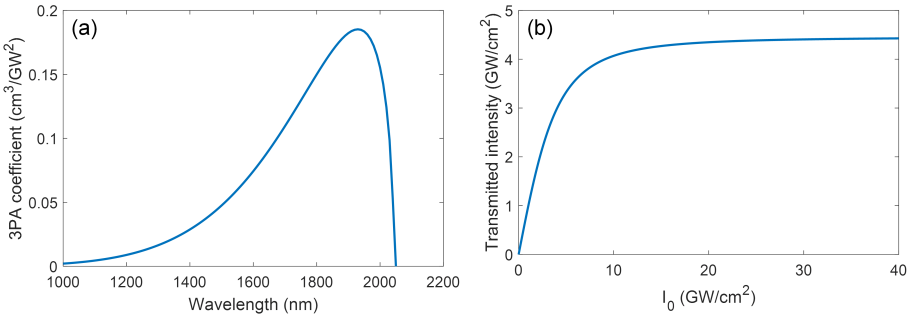

Fig. 3. (a) Calculated 3PA coefficient vs. wavelength for $Al_{0.32}Ga_{0.68}As$. (b) Calculated transmitted intensity vs. intial intensity I_0 for light propagating in an $Al_{0.32}Ga_{0.68}As$ waveguide at 1560 nm, using the 3PA coefficient from (a).

thermal conductivity, the membrane width could be substantially reduced to allow a shorter path to the much more thermally conductive silicon substrate.

4.6. Nonlinear losses

For applications in frequency conversion and spectrum broadening that will rely on 1550-nm pulsed laser sources, the effects of nonlinear absorption are important to consider. With the $Al_{0.32}Ga_{0.68}As$ composition used in this work, two-photon absorption (TPA) will not occur for pump wavelengths longer than 1362 nm, allowing significant broadening of a 1560 nm pump before any TPA is observed. However, three-photon absorption (3PA) is still a significant effect, due to its relatively large coefficient in AlGaAs [7]. Using the model for scaling rules of 3PA absorption in AlGaAs presented in Ref. [8], we have plotted the calculated absorption for $Al_{0.32}Ga_{0.68}As$ in Fig. S3(a). At 1560 nm, its 3PA coefficient has a value of 0.063 cm^3GW^{-2}, which is similar to the value of 0.065 cm^3GW^{-2} for lower-Al compositions such as $Al_{0.18}Ga_{0.82}As$. Mainly, the peak value and the peak absorption wavelength are lowered and blue-shifted for higher Al content. Considering the absorption effects of 3PA alone, the on-chip normalized

transmission can be modeled as

$$\frac{dI}{dz} = -\alpha_3 I^3, \tag{3}$$

where I is the intensity in the waveguide, z is the distance in the propagation direction, and α_3 is the 3PA coefficient [7]. Solving Eq. S3 for the case of $I(0) = I_0$ where I_0 is the initial waveguide-coupled intensity, we obtain

$$I(z) = \frac{1}{\sqrt{2\alpha_3 z + \frac{1}{I_0^2}}}. \tag{4}$$

In the case of a 4 mm long waveguide (as we used in the case of near-IR supercontinuum generation), we have plotted Eq. S4 for different I_0 in Fig. S3(b). It can be seen that for waveguide-coupled intensities greater than 10 GW/cm^2, the output is heavily saturated. In the supercontinuum experiments in Sec. 2.3.1 of the manuscript, not much change was observed in the shape of the spectrum beyond 3.4 pJ of pulse energy, corresponding to about 20 GW/cm^2 peak pulse intensity, averaged over the waveguide mode area. This is in fairly good agreement and lends credibility to the notion that the spectrum bandwidth is currently limited by 3PA.

4.7. Substrate leakage

Finally, we briefly comment on the cutoff wavelength achieved for the waveguide/platform geometry presented in this work. This particular suspended geometry supports waveguiding over a large optical bandwidth thanks to the nearly symmetric environment (except for the membrane's slab) and strong index contrast. Considering the waveguide used for supercontinuum generation in the mid-IR, with a width of 2.15 um, eigenmode simulations show that leakage into the sides of the trenches becomes noticeable at a value of 0.4 dB/cm at 7 μm. At 7.5 μm, a leakage loss of 3.5 dB/cm is simulated. A true mode cutoff is not observed before leakage losses become excessive. We also note that larger trench widths can be employed to mitigate leakage losses for applications requiring long-wave operation.

5. Measurement setups

Here, we provide additional details on the measurement setups utilized in the experiments. The main configurations are shown in Fig. S4. In all cases, the polarization of the laser light was oriented parallel to the table to excite the quasi-TE mode of the waveguides. The setup in Fig. S4(a) was used for the 1550-pumped supercontinuum experiments (asphere NA = 0.6, lensed fiber mode field diameter = 2.5 μm). Using a lensed fiber at the output allowed higher-efficiency broadband collection of light compared to a lens. The setup in Fig. S4(b) was used for microring resonator measurements and coupling loss tests for λ = 1260, 1550 and 2400 nm (asphere NA = 0.6). Alignment was performed at near-IR wavelengths using the Vidicon camera, after which a reflective collimator was substituted into the beam path and used to collect the output into a 50 μm-core multi-mode silica fiber. The setup in Fig. S4(c) was used for 3060 nm pumping experiments (asphere NA = 0.56). The setup in Fig. S4(d) was used for microring resonator analysis at λ = 3.6 μm using the idler beam output of an optical parametric oscillator (OPO). Because of the erratic nature of wavelength tuning using etalon angles, a wavemeter was aligned to the input path to periodically check wavelength as needed. Finally, the setup in Fig. S4(e) was used for microring resonator analysis at λ = 4.6 μm. Using laser pump current modulation at a fixed temperature, a wavelength tuning range of about 8 nm was achieved. The beam exiting the QCL was magnified 3× with a Galilean beam expander, to better match the 6 mm clear aperture of the asphere (NA = 0.56). The polarization was rotated to TE using a half-wave plate prior to coupling into the waveguide. For all setups used for measuring coupling loss, the experiment was

performed in four steps: (1) measure the absolute power transmission through the device under test with a power meter, (2) measure the absolute power transmission through the same path with no device in place (the light was simply coupled through both identical aspheric lenses), (3) calculate transmission as the ratio of these two quantities, and (4) factor out any relevant propagation losses (usually negligible, except for the case of $\lambda = 4.6$ μm). The final loss per edge coupler is then half of the total loss.

References

1. B. Guha, F. Marsault, F. Cadiz, L. Morgenroth, V. Ulin, V. Berkovitz, A. Lemaître, C. Gomez, A. Amo, S. Combrié, B. Gérard, G. Leo, and I. Favero, "Surface-enhanced gallium arsenide photonic resonator with quality factor of 6x10ˆ6," Optica **4**, 218–221 (2017).
2. D. W. Sheibley and M. H. Fowler, "Infrared spectra of various metal oxides in the region of 2 to 26 microns." https://ntrs.nasa.gov/archive/nasa/casi.ntrs.nasa.gov/19670003469.pdf (1966).
3. W. G. Spitzer and J. M. Whelan, "Infrared Absorption and Electron Effective Mass in n-Type Gallium Arsenide," Phys. Rev. **114**, 59–63 (1959).
4. V. Verlaan, C. H. M. van der Werf, W. M. Arnoldbik, H. D. Goldbach, and R. E. I. Schropp, "Unambiguous determination of Fourier-transform infrared spectroscopy proportionality factors: The case of silicon nitride," Phys. Rev. B **73**, 195333 (2006).
5. B. Bendow, H. G. Lipson, and S. P. Yukon, "Multiphonon absorption in highly transparent semiconducting crystals," Phys. Rev. B **16**, 2684 (1977).
6. D. T. Spencer, J. F. Bauters, M. J. R. Heck, and J. E. Bowers, "Integrated waveguide coupled Si3N4 resonators in the ultrahigh-Q regime," Optica **1**, 153 (2014).
7. J. U. Kang, A. Villeneuve, J. S. Aitchison, and G. I. Stegeman, "Nonlinear optics of semiconductors near the half band gap," in *Ultrafast Phenomena in Semiconductors IV,* vol. 3940 (International Society for Optics and Photonics, 2000), pp. 53–64.
8. B. S. Wherrett, "Scaling rules for multiphoton interband absorption in semiconductors," J. Opt. Soc. Am. B **1**, 67–72 (1984).

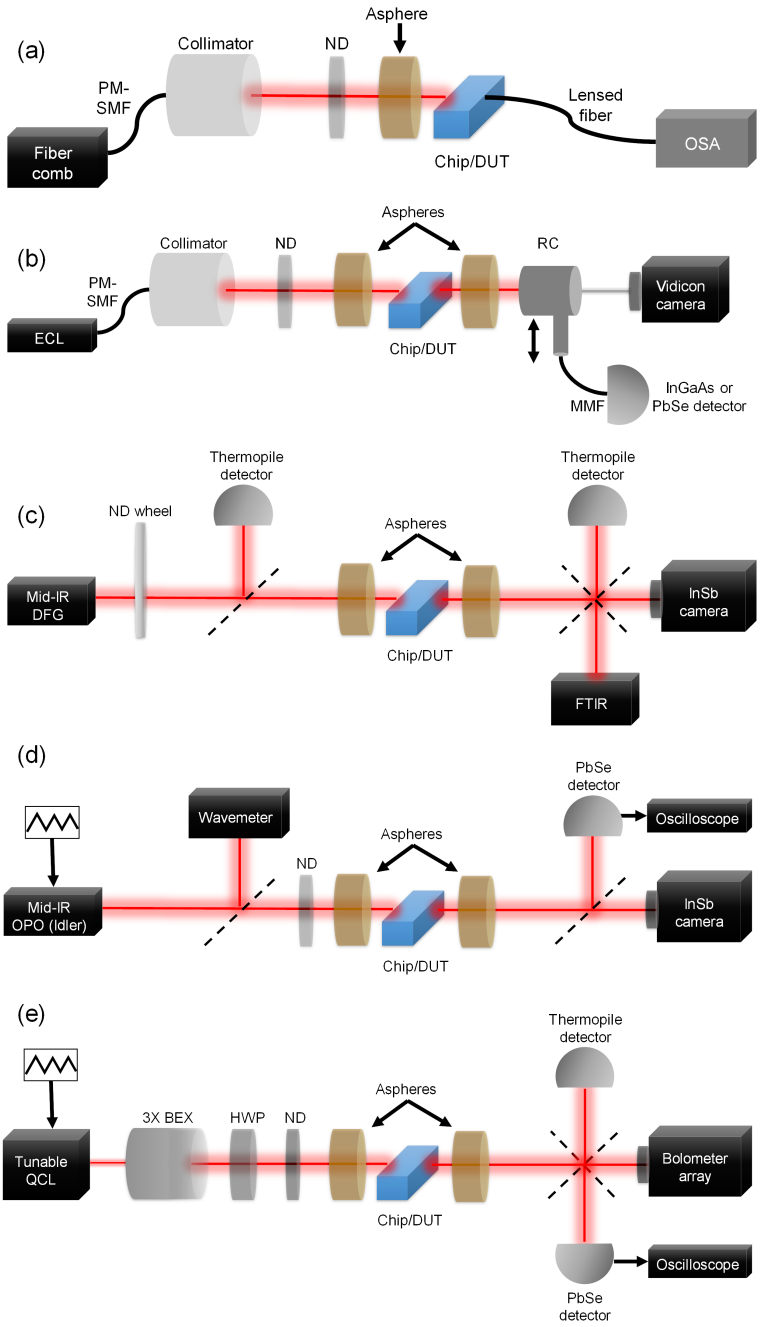

Fig. 4. Measurement setups used in the experiment. (a) 1550 nm-pumped supercontinuum; (b) micro-ring resonator analysis at 1260, 1550 and 2400 nm; (c) 3060 nm-pumped supercontinuum; (d) micro-ring resonator analysis at 3600 nm; (e) micro-ring resonator analysis at 4600 nm. PM-SMF: polarization-maintaining single-mode fiber; ND: neutral-density filter; DUT: device under test; OSA: optical spectrum analyzer; ECL: external cavity laser; RC: reflective collimator; MMF: multimode fiber; BEX: beam expander; HWP: half-wave plate.